



Master's thesis  
Your Field

# Formation of cores by merging supermassive black holes

Joonas Suortti

July 29, 2019

Tutor: prof. Smith

Censors: prof. Smith  
doc. Smythe

UNIVERSITY OF HELSINKI  
DEPARTMENT OF SOMETHING

PL 42 (Kuvitteellinen katu 1)  
00014 Helsingin yliopisto

“Bachelor’s degrees make pretty good placemats if you get them laminated.”

—Jeph Jacques



# Contents

<b>1</b>	<b>Introduction</b>	<b>1</b>
<b>2</b>	<b>Theory</b>	<b>2</b>
<b>3</b>	<b>KETJU</b>	<b>3</b>
3.1	Chain and Tree-code Regions . . . . .	3
3.1.1	AR-CHAIN . . . . .	3
3.1.2	GADGET-3 . . . . .	3
<b>4</b>	<b>Merger Simulations Using KETJU</b>	<b>4</b>
4.1	Simulation Details . . . . .	4
4.2	Black Hole Trajectories . . . . .	7
4.3	Core Size Measurements . . . . .	9
4.4	Velocity Anisotropy . . . . .	13
4.5	Line-of-Sight Kinematics . . . . .	15
4.6	Comparison to NGC 1600 . . . . .	21
<b>5</b>	<b>Conclusions</b>	<b>24</b>
<b>A</b>	<b>Figures</b>	<b>25</b>
	<b>Bibliography</b>	<b>31</b>

# 1. Introduction

## 2. Theory

## **3. KETJU**

Description of basic functionality: what KETJU does, why it's created, basic description of the multiple integration region system.

### **3.1 Chain and Tree-code Regions**

#### **3.1.1 AR-CHAIN**

#### **3.1.2 GADGET-3**

# 4. Merger Simulations Using KETJU

We study the formation of cored galaxies through galaxy mergers by analysing the results from two sets of KETJU simulations (Rantala et al., 2018; Mannerkoski et al., 2019). The merger progenitor galaxies in these simulations contain central supermassive black holes. During the merger event, the SMBHs form a hardening binary, a likely source for the observed cores. We try to determine if there is a connection between the binary SMBH and the existence of a light deficient core, and if the KETJU results are comparable to observations.

## 4.1 Simulation Details

All of the analysed simulation runs use merger progenitor galaxies from the same progenitor pool. There are seven different progenitors in total. Six of them (BH-1 - BH-6) contain central supermassive black holes, with the SMBH masses varying from  $8.5 \times 10^8 M_\odot$  to  $8.5 \times 10^9 M_\odot$ . The seventh progenitor (BH-0) doesn't contain an SMBH in its centre, and is included simply for the sake of comparison. The masses of the progenitors' central SMBHs are listed in table 4.1.

Apart from the SMBH masses however, all of the progenitor galaxies have identical physical properties. These properties, which are motivated by observations and dynamical simulations of NGC 1600 (Rantala et al., 2018), are described in table



Progenitor	$M_{\bullet} [\times 10^9 M_{\odot}]$
BH-0	-
BH-1	0.85
BH-2	1.7
BH-3	3.4
BH-4	5.1
BH-5	6.8
BH-6	8.5

**Table 4.1:** Central SMBH masses of the progenitors used in the simulations.

#### 4.2.

Alongside the physical properties, the distributions of the different particles, that make up the progenitor galaxies, are also identical. The progenitors' central SMBHs are simply modelled as point masses, located in the origin of their internal coordinate system; they don't contain any gas (i.e. the simulations describe so called "dry" mergers); and the stellar and dark matter particles are distributed according to a Dehnen density-potential model (Dehnen, 1993):

$$\rho(r) = \frac{(3 - \gamma)M}{4\pi} \frac{a}{r^{\gamma}(r + a)^{4-\gamma}}, \quad (4.1)$$

$$\phi(r) = \frac{GM}{a} \times \begin{cases} -\frac{1}{2-\gamma} \left[ 1 - \left( \frac{r}{r+a} \right)^{2-\gamma} \right] & \gamma \neq 2 \\ \ln \frac{r}{r+a} & \gamma = 2 \end{cases}, \quad (4.2)$$

where  $M$  is the total mass,  $a$  is a scaling radius, and  $\gamma$  is the central slope of the profile. For stellar particles  $\gamma = 3/2$ , while for the dark matter particles  $\gamma = 1$ .

While the merger progenitor galaxies are the same, the initial conditions of the simulations are quite different. The Mannerkoski et al. (2019) simulations comprise of four consecutive runs, where the initial run merges the progenitor galaxies BH-6

$M_\star$	$R_e$	$M_{\text{DM}}$	$f_{\text{DM}}(r_{1/2})$	$N_\star$	$N_{\text{DM}}$
$[\times 10^{11} M_\odot]$	[kpc]	$[\times 10^{13} M_\odot]$			
4.15	7	7.5	0.25	$4.15 \times 10^6$	$1.0 \times 10^7$

**Table 4.2:** The constant physical properties of the progenitors: $M_\star$ : Stellar mass $R_e$ : Effective radius $M_{\text{DM}}$ : Dark matter halo mass $f_{\text{DM}}(r_{1/2})$ : The fraction of dark matter mass from the total mass inside the effective radius $N_\star$ : Number of stellar particles $N_{\text{DM}}$ : Number of dark matter particles

and BH-2 (table 4.1) with each other, while the subsequent runs swap BH-6 for the merger remnant from the previous simulation. On the other hand, the simulations done by Rantala et al. (2018) simply comprise of seven different mergers between two of the same type of progenitor galaxies. Table 4.3 shows the central SMBH masses of the progenitors used in each simulation run.

Like the initial conditions, the type of results gathered from the two sets of simulations also differ from each other. From the simulations done by Mannerkoski et al. (2019); only the locations, velocities and masses of the central SMBHs are saved. This data comes from time steps starting from when the semi-major-axis of the merging SMBH binary is  $a \lesssim 5000R_s$  ( $R_s$  is the Schwarzschild radius) up until the separation between the black holes is  $\lesssim 100R_s$ . However, the results from the simulations done by Rantala et al. (2018) not only include the velocities, positions and masses of the black holes; but also of the stellar and dark matter particles. These results, in turn, are given in the form of a single snapshot at the simulation time  $t = 2\text{Gyr}$ . Due to the distinct difference between the type of results gained from the two different simulation sets (and for simplicity's sake) we will, from now on, be calling the simulations from Mannerkoski et al. (2019) "Runs" and the ones

Mannerkoski et al. (2019)			Rantala et al. (2018)		
Run	$M_{\bullet,1}[10^9 M_{\odot}]$	$M_{\bullet,2}[10^9 M_{\odot}]$	Snapshot	$M_{\bullet,1}[10^9 M_{\odot}]$	$M_{\bullet,2}[10^9 M_{\odot}]$
1	8.5	1.7	0	-	-
2	10.2	1.7	1	0.85	0.85
3	11.9	1.7	2	1.7	1.7
4	13.6	1.7	3	3.4	3.4
			4	5.1	5.1
			5	6.8	6.8
			6	8.5	8.5

**Table 4.3:** Central SMBH masses of the progenitors used in the different simulation runs.

from Rantala et al. (2018) "Snapshots" (as is also done in table 4.3).

## 4.2 Black Hole Trajectories

Since we are trying to determine if merging SMBH binaries form cores in merger remnants, we must make sure that the progenitors' central black holes actually merge in our simulations. This is done by looking at the "Run" simulations, as they contain the locations of the black holes from multiple time steps, and as the "Snapshots" still show both of the SMBHs.

Plotting the positions of the black holes from "Run 3" in coordinates centred on the binary's centre-of-mass during the initial time step gives us figure 4.1. Even by eye, one can clearly see that the orbit of the black hole with a smaller mass becomes smaller and smaller as the binary moves further away from its initial position. While this doesn't explicitly tell us that the black holes merge into each other, it does indicate the existence of a hardening process in the binary. Similar figures to figure 4.1 from all four "Runs" can be found in the appendix (figure A.1).

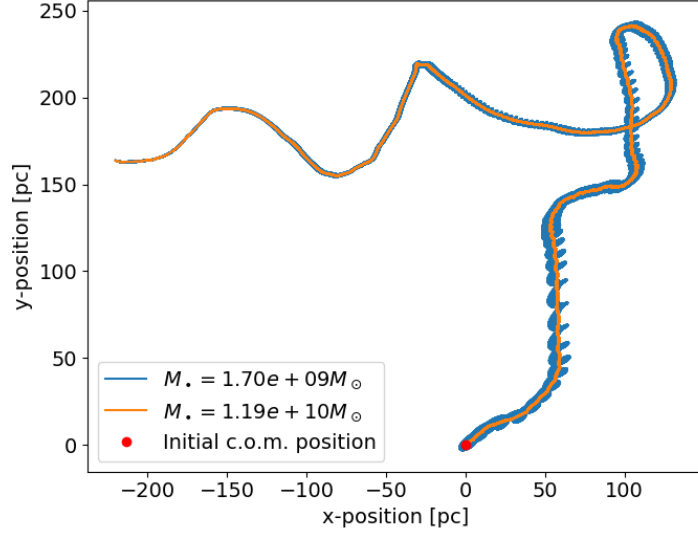


**Figure 4.1:** The trajectories of the black holes during "Run 3". The coordinates are centred on the initial location of the centre-of-mass of the binary black hole. The orange and blue lines show the paths taken by the smaller and larger black holes respectively. Both paths show clear spiral patterns which become smaller and smaller as the simulation proceeds. The paths end at the location where the black holes merge, i.e. where the distance between them is  $\lesssim 100R_s$  ( $R_s$  is the Schwarzschild radius).

The most likely obstacle for the complete merging of the binary black holes is the so-called final-parsec problem; where due to the lack of stellar material that can be ejected during the three-body scattering phase, the hardening of the binary stops when the separation between the two black holes is  $\sim 1\text{pc}$ . This is assumed to happen since not only is the binary constantly ejecting the finite amount of stars inside the loss cone (defined in section 2), but the loss cone itself is becoming smaller due to the contracting binary orbit.

Figure 4.2 shows the time evolution of both the semi-major axis and the eccentricity of the binary orbits from all of the simulation runs. Interestingly enough the semi-major axes of all of the binaries go far below single parsec scales, meaning that the final-parsec problem doesn't seem to play a part in the simulations. This

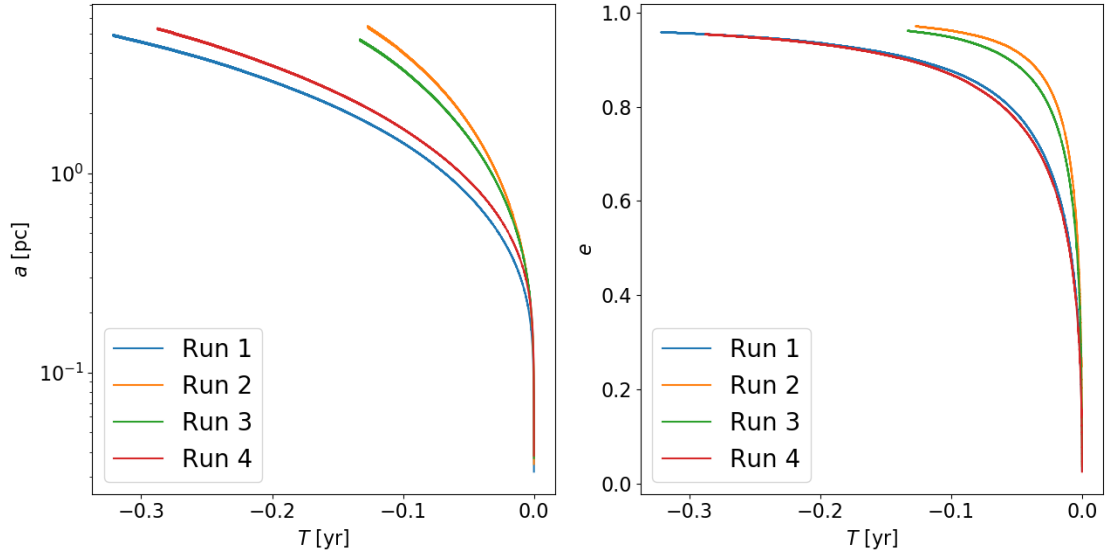


**Figure 4.2:** The semi-major axes (left) and eccentricities (right) of the black hole systems in the simulations "Runs 1"- "Run-4" as a function of time. The zero position on the x-axis corresponds to the point in simulation time, where the black hole merging event occurs.

implies that, there exists some loss cone refill mechanism which allows the binary to eject more stellar material than what initially exists inside the loss cone.

### 4.3 Core Size Measurements

In order to check if a galaxy is cored or not, we have to calculate its surface brightness profile, and check if the galaxy contains surface brightness deficiencies near its centre. As the "Runs" don't contain stellar data, we use the "Snapshots" for this core analysis.

We calculate the surface brightness profiles from the snapshots by: changing the coordinate system to centre-of-mass coordinates, projecting the stellar particles onto a plane, and calculating the mass inside logarithmically spaced radial bins to get a radial surface mass density profile. We then do the aforementioned calculations 100 times from random viewing angles, and get 100 different density profiles. These profiles are then averaged azimuthally, which allows us to form a smooth mass surface

density profile, that can be turned into a surface brightness profile by assuming a mass-to-light ratio of  $M/L = 4$  (Rantala et al., 2018).

In figure 4.3, one can see example surface brightness profiles for all of the snapshots. Looking at the different curves, it seems like the presence of central SMBHs in the merger progenitors does cause some kind of brightness deficiency near the merger remnants centre. Not only that, the higher the mass of the central black holes, the larger the surface brightness deficiency seems to be.

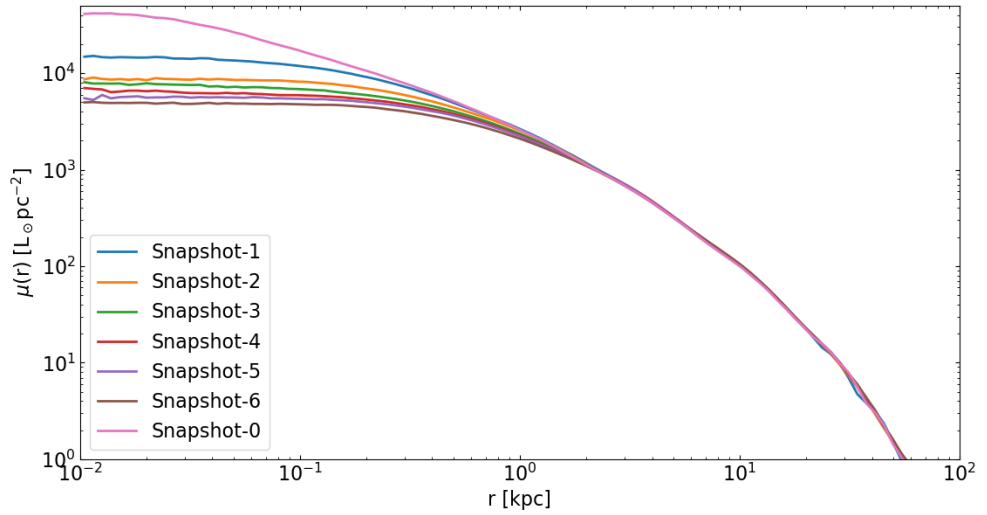


**Figure 4.3:** Surface brightness profiles from every snapshot. These were calculated by dividing the simulated galaxy remnants into 100 radial logarithmic bins, and averaging the surface brightness inside the bins through 100 random viewing angles. The luminosity of the particles was estimated by assuming a mass-to-light ratio of  $M/L = 4$ .

The deficiencies found in the surface brightness profiles imply the presence of cores, however determining the precise size of the core requires us to find the exact location where the deviations from the expected power-law profile start. This can be done by fitting the calculated profile with a model that is a combination of two power laws: a shallow inner power-law, and a steeper outer power-law. The radius at which the power laws shift, i.e. the break radius  $r_b$ , is equivalent to the radius of

the core.

There are two commonly used options for modelling the surface brightness profiles. The first one is the core-Sérsic profile (Graham et al., 2003a), which can be expressed using the following equation:

$$\mu(r) = \mu' \left[ 1 + \left( \frac{r_b}{r} \right)^\alpha \right]^{\gamma/\alpha} \exp \left\{ -b_n [(r^\alpha + r_b^\alpha) / r_e^\alpha]^{1/(\alpha n)} \right\}, \quad (4.3)$$

where  $r_b$  is the break radius,  $\gamma$  is the logarithmic slope of the inner power-law,  $\alpha$  controls the sharpness of the transition between the two power-laws,  $r_e$  and  $n$  are the effective half-mass radius and the Sérsic index of the outer power-law, and the normalization factor  $\mu'$  is defined by:

$$\mu' = \mu_b 2^{-\gamma/\alpha} \exp \left[ b_n \left( 2^{(1/\alpha)} r_b / r_e \right)^{1/n} \right], \quad (4.4)$$

where  $\mu_b$  is the surface brightness at the break radius.

The second option is using the so called Nuker profile (Lauer et al., 1995):

$$\mu(r) = 2^{(\beta-\gamma)/\alpha} \mu_b \left( \frac{r_b}{r} \right)^\gamma \left[ 1 + \left( \frac{r}{r_b} \right)^\alpha \right]^{(\gamma-\beta)/\alpha}, \quad (4.5)$$

where  $r_b$  is once again the break radius,  $\mu_b$  is the surface brightness at the break radius,  $\beta$  and  $\gamma$  are the logarithmic slopes of the power-laws inside and outside of the break radius respectively, and  $\alpha$  is the sharpness of the transition between the two slopes.

We calculate the core radii of the merger remnants by using the "Levenberg-Marquardt" fitting algorithm to fit both the core-Sérsic model and the Nuker model to the remnant's surface brightness profile. Figure 4.4 shows a comparison of the resulting fits for snapshot 3 (refer to table 4.3), while figures A.2 and A.3, located in the appendix, show the fits for every snapshot that contains SMBH binaries. The values of the best-fit parameters are written on the figures, and looking at them, it is clear that the exact value of the best-fit break radius, i.e. the core radius estimate, depends quite heavily on the used model.

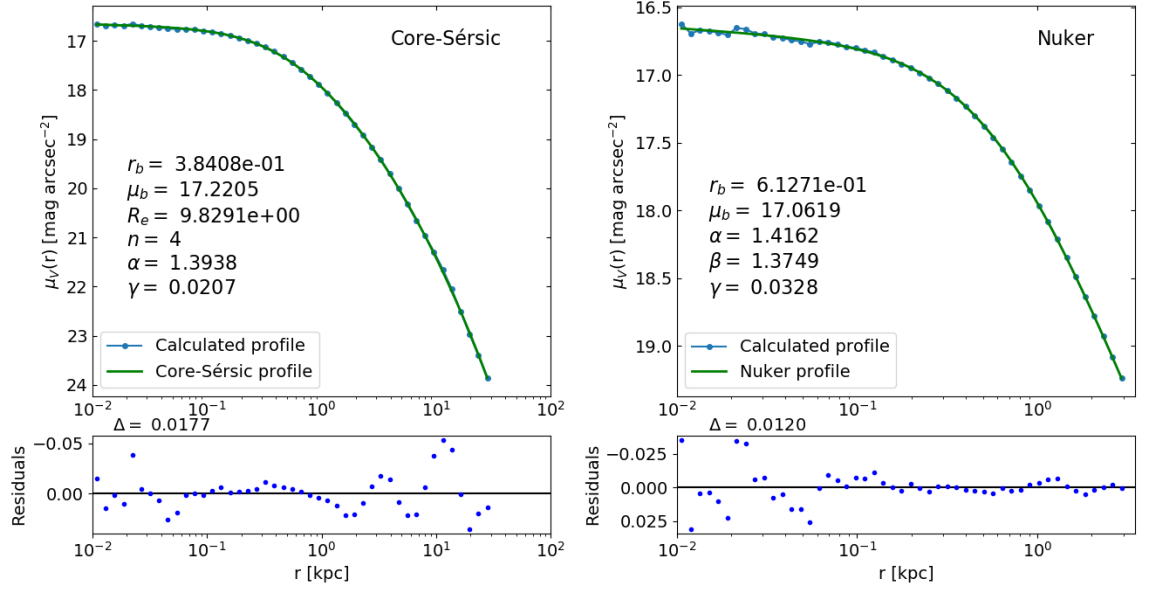


**Figure 4.4:** Core-Sérsic and Nuker profile fits of surface brightness profiles calculated from Snapshot 3 (top-left and top-right figures). The best fit parameters are written on the figures, and are in the same units as the axes (i.e.  $r_b$  and  $R_e$  in kilo-parsecs, and  $\mu_b$  in V-band magnitudes per arc-second squared). The relative residuals of the fits are plotted under their respective figures. The delta describes the root-mean-square of the residuals.

Which model is better for estimating the size of the core is up for debate (Lauer et al., 2007b; Dullo and Graham, 2012). While the RMS of the relative residuals seems to be consistently (although just marginally) smaller for the Nuker model when compared to the RMS for the core-Sérsic model (compare figures A.2 and A.3), one also has to take into account that in the Nuker model the best-fit value for  $r_b$  is highly dependent on the fitting range (Graham et al., 2003b). Furthermore, as stated by Rantala et al. (2018), in order to get sensible values for all of the model parameters, the fitting range of the Nuker model has to be narrowed down closer to the galactic core ( $\alpha \lesssim 1$  might prevent the model from describing the profile as a combination of two power-laws).

One could also estimate the size of the core without model fitting by using the so-called "cusp radius"  $r_\gamma$ , which is the radius at which the negative logarithmic slope of the surface brightness profile  $\gamma'$  equals 1/2 (Carollo et al., 1997; Lauer et al.,



2007a). The cusp radius  $r_\gamma$  is also an estimation for the location where the inner power-law of the profile changes into the outer power-law, and thus equates to the core radius.

We calculate  $r_\gamma$  for all of the snapshots with SMBH binaries by calculating the first derivative (gradient) of the surface brightness profiles, and then using a "Nelder-Mead" minimization algorithm to find the radius, at which the gradient gets the value  $-1/2$ .

Figure 4.5 compares the core radius estimates from each of the three methods for every merger remnant from the snapshots. The break radii from the Nuker fits are consistently larger than the other core radius estimates, while also being the ones that, in general, agree least with the other values. Nevertheless, a clear trend of the size of the core growing with the merger progenitors' central SMBH masses can be seen.

## 4.4 Velocity Anisotropy

One way of adding to the evidence that a galaxy has formed a core through core scouring by binary black holes, is to study its velocity anisotropy profile defined in Binney and Tremaine (2008):

$$\beta(r) = 1 - \frac{\sigma_\theta^2 - \sigma_\phi^2}{2\sigma_r^2} = 1 - \frac{\sigma_t^2}{\sigma_r^2}, \quad (4.6)$$

where  $\sigma_\theta$ ,  $\sigma_\phi$  and  $\sigma_r$  are velocity dispersions in the spherical coordinates, and  $\sigma_t = \sqrt{(\sigma_\theta^2 + \sigma_\phi^2)/2}$  is the tangential velocity dispersion. The  $\beta$  parameter describes the relation between objects in radial and tangential orbits around the black hole binary, where a negative  $\beta$  shows an abundance of tangential orbits, and positive an abundance of radial orbits.

Figure 4.6 shows  $\beta$ -profiles calculated from all of the merger remnant snapshots using equation 4.6. According to the profiles, the outer areas of the remnants

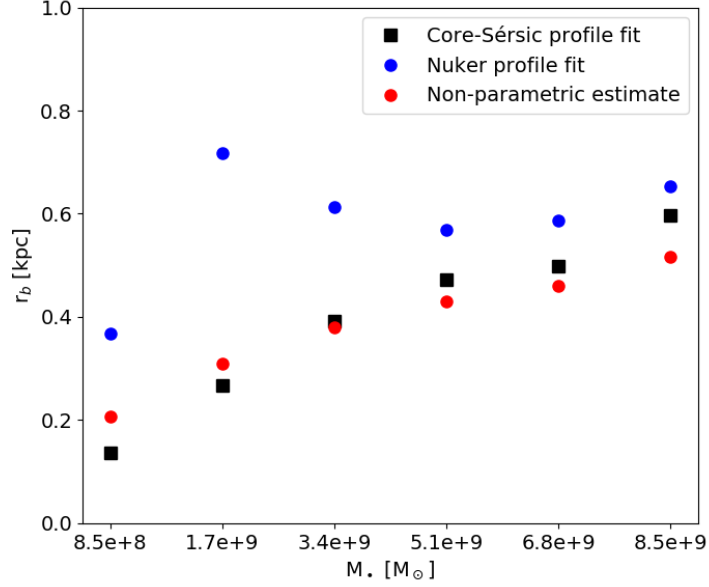


**Figure 4.5:** Comparison of the core radii of the merger remnants, gained through three different methods: Core-Sérsic profile fitting (black squares), Nuker profile fitting (blue circles) and finding the "cusp radius" (red circles). The x-axis shows the masses of the central SMBHs of the merger progenitors.

are dominated by radial orbits, while the majority of orbits near the centre are tangential.

As the merging of two galaxies would cause a randomization of the stellar orbits, an area with negative  $\beta$  in the merger remnant, would imply that the stars on radial orbits have been ejected from the system. It has been shown that hardening black hole binaries can eject stars on highly radial orbits from the galactic core, which can then in turn cause the outer orbits to become more radial (Quinlan and Hernquist, 1997; Milosavljević and Merritt, 2001; Thomas et al., 2014).

This could certainly be the reason behind the shapes of the  $\beta$  profiles seen in figure 4.6. It is clear that the presence of an SMBH binary has an effect on the profiles' shape, as not only is the profile for the merger without a binary the only one completely dominated by radial orbits, but the larger the binary's mass, the

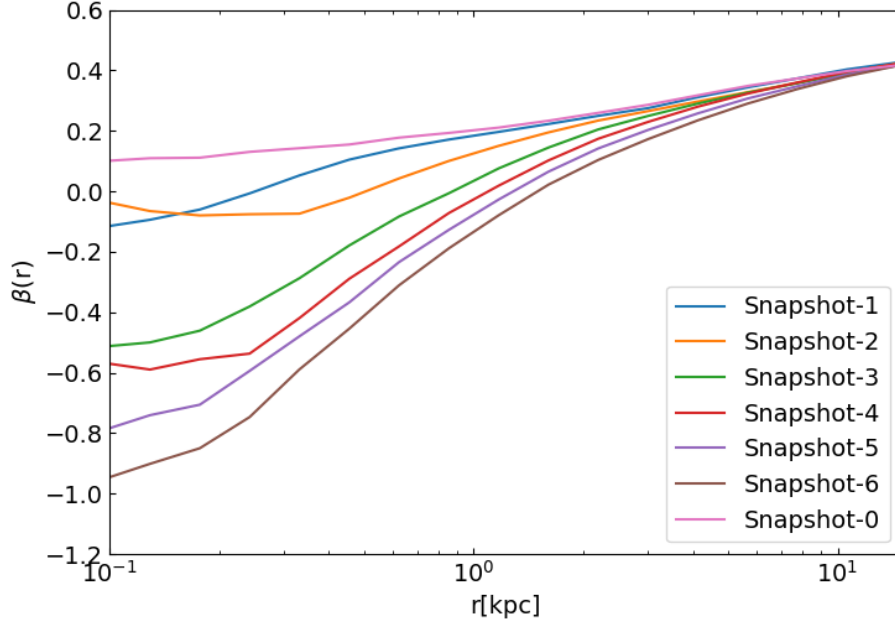


**Figure 4.6:** Velocity anisotropy (beta) profiles of the merger remnant in every snapshot.

steeper the slope of the profile. These properties of the profiles also make sense in the context of ejection of stellar particles by hardening black hole binaries. The larger the masses of the SMBHs in the binary are, the larger the gravitational sphere-of-influence of the binary is, which results in more of the radially orbiting stellar particles being ejected.

## 4.5 Line-of-Sight Kinematics

In order to make sure that the KETJU simulations produce results equivalent to observations, we analyse the line-of-sight (LOS) kinematics of the "snapshots". We will be analysing four different LOS velocity distribution properties: the average LOS velocity  $V_{\text{avg}}$ , the velocity dispersion  $\sigma$ , and the  $h_3$  and  $h_4$  parameters which correspond to the skewness and the kurtosis of the distribution respectively. The distribution from which these properties are calculated is defined as the following

modified Gaussian function (Rantala et al., 2018):

$$f(v) = I_0 e^{-\gamma^2/2} (1 + h_3 H_3(y) + h_4 H_4(y)), \quad (4.7)$$

where  $I_0$  is a normalization constant,  $\gamma$  is the central slope of the particle density profile,  $y = (v - V_{\text{avg}})/\sigma$ , and  $H_3$  and  $H_4$  are the third and fourth order Hermite polynomials respectively:

$$H_3(y) = (2\sqrt{2}y^3 - 3\sqrt{2}y) / \sqrt{6}, \quad (4.8)$$

$$H_4(y) = (4y^4 - 12y^2 + 3) / \sqrt{24}. \quad (4.9)$$

In order to calculate the above properties, we first define the "line-of-sight" as the intermediate axis of the merger remnants, and orient the remnant accordingly using the inertia tensor. Next, we divide a 2D line-of-sight projection of the remnant into "spaxels" (or simply bins), using the voronoi tessellation algorithm (Cappellari and Copin, 2003). The shape and size of the spaxels are determined so that each one contains the same signal-to-noise ratio, which in our case is defined as the number of stellar particles. The LOS-velocities inside the spaxels are then made into a histogram, into which we fit the modified Gaussian function described in equation 4.7, giving us the values of the LOS-velocity distribution parameters:  $V_{\text{avg}}$ ,  $\sigma$ ,  $h_3$  and  $h_4$  for the spaxel in question. Finally, the values of the spaxels can be plotted, giving us 2D voronoi binned maps of all of the four parameters.

Figure 4.7 shows the voronoi binned 2D maps of the four LOS velocity distribution parameters for snapshot-0 and snapshot-6, as well as luminosity contours with one magnitude spacing. Similar maps for all of the merger remnant snapshots are in figures A.4 and A.5 in the appendix.

The IFU maps in figures A.4 and A.5 show that the line-of-sight kinematics of the simulated merger remnants are far from isotropic, with some of the maps from simulations with larger central SMBHs showcasing counter-rotating central regions, or "kinematically distinct cores" (KDC). These features, alongside the relatively low

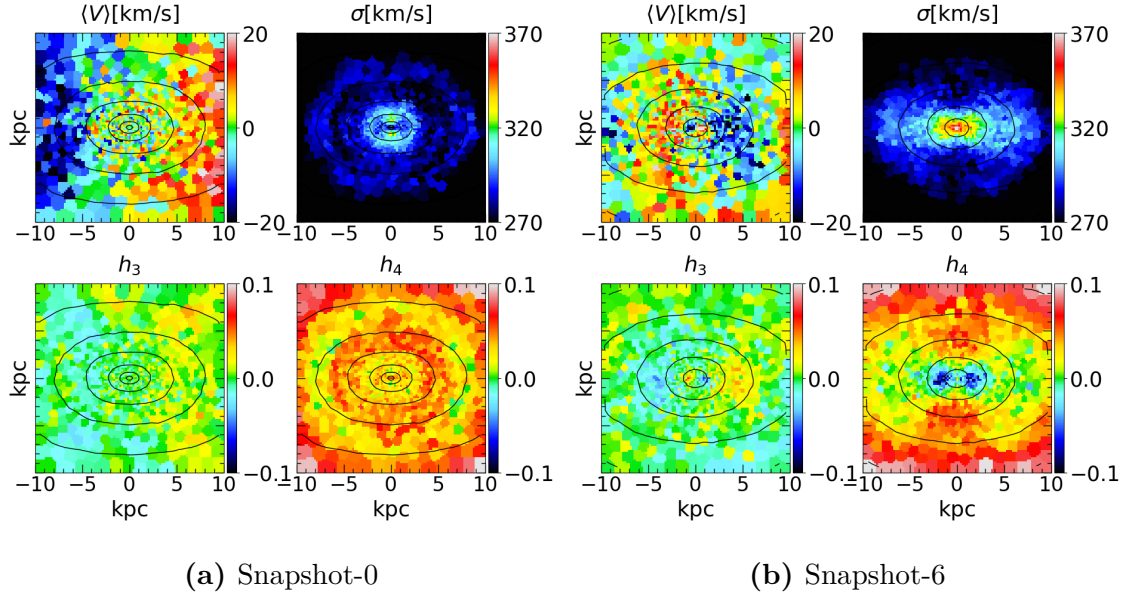


**Figure 4.7:** IFU-maps of average LOS-velocities, velocity dispersion,  $h_3$  parameters and  $h_4$  parameters from two simulated merger remnants. The four maps on the left are from Snapshot-0 and the four on the right are from Snapshot-6.

average LOS-velocities, are found in galaxies called "slow rotators" (Emsellem et al., 2007). Slow rotator galaxies are early type galaxies which are assumed to have been formed through gas-poor "dry" mergers (Emsellem et al., 2007; Cappellari et al., 2007); processes not unlike the ones simulated in our simulations. As such, the merger remnants being slow rotators is a somewhat expected result, however it nonetheless implies that the KETJU simulations do produce physically accurate results.

Further analysis of the nature of the simulated mergers' rotation can be done by looking at the  $\lambda_R$  parameter, which describes the angular momentum of a galaxy (Emsellem et al., 2007). More importantly, the parameter allows us to differentiate between the aforementioned slowly rotating galaxies and so-called fast rotators (see figure 4.8) (Emsellem et al., 2007). The parameter itself is defined in a general form as:

$$\lambda_R \equiv \frac{\langle R|V| \rangle}{\langle R\sqrt{V^2 + \sigma^2} \rangle}, \quad (4.10)$$

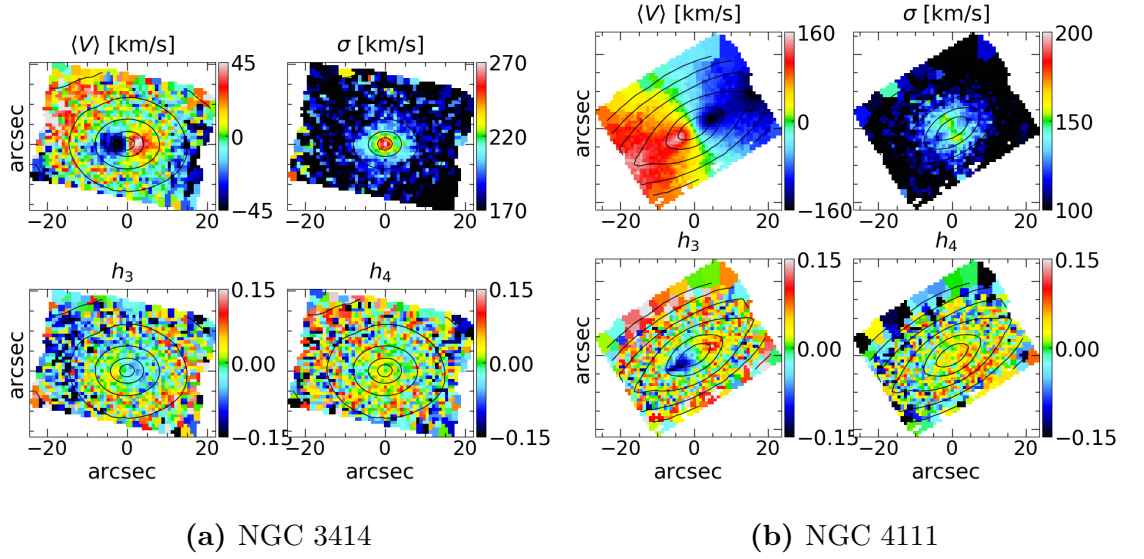


**Figure 4.8:** Comparison between the IFU-maps of a known slow (NGC 3414) and fast rotator (NGC 4111) galaxies from the ATLAS<sup>3D</sup> survey. The maps show the average LOS-velocities, velocity dispersion,  $h_3$  parameters and  $h_4$  parameters of NGC 3414 (Emsellem et al., 2004) and NGC 4111 (Cappellari et al., 2011).

where  $R$  is the projected distance from the galactic centre,  $V$  is velocity,  $\sigma$  is the velocity dispersion, and  $\langle \rangle$  denote that the nominator and denominator of the equation are velocity weighted means. However, as most of the observational kinematic analysis of galaxies is done through binned 2D spectroscopy, and as the IFU-maps made from our simulations are produced the same way as the ones gained through observations, we will be using the following version of the equation:

$$\lambda_R = \frac{\sum_{i=1}^{N_p} F_i R_i |V_i|}{\sum_{i=1}^{N_p} F_i R_i \sqrt{V_i^2 + \sigma_i^2}}, \quad (4.11)$$

where  $F_i$ ,  $R_i$ ,  $V_i$  and  $\sigma_i$  are the flux, projected distance from the galaxy centre, velocity and velocity dispersion of the  $i$ th bin, and  $N_p$  is the number of bins. In the case of our simulations, the  $N_p$  bins used are of course the voronoi bins described earlier in this section.

Determining whether a galaxy is either a fast or a slow rotator using  $\lambda_R$  is done by comparing the value that the parameter gets at the galaxy's effective radius, to

some pre-defined threshold. The original threshold used for differentiating the two rotator types is:  $\lambda_{Re} < 0.1$ , where  $\lambda_{Re}$  is  $\lambda_R$  at the effective radius, and where galaxies fulfilling the condition are classified as slow rotators (Emsellem et al., 2007). Later revisions by Emsellem et al. (2011) and Cappellari (2016) take the ellipticity ( $\epsilon$ ) of the galaxy into account, and define the threshold as being either  $\lambda_{Re} < 0.31\sqrt{\epsilon}$  or  $\lambda_{Re} < 0.08 + \epsilon/4$  for  $\epsilon < 0.4$  respectively. Through including the ellipticity in the threshold, the revisions account for increased anisotropy in the kinematics of flatter galaxies. The latter threshold then improves on the former by reducing the risk of misidentifying round non regular slow rotators as fast rotators.

Since two of the three aforementioned slow rotator thresholds require us to know the ellipticity of the galaxy, we calculate the simulated merger remnants' ellipticities before analysing their rotation. The ellipticity calculations are done using a method described in Zemp et al. (2011), which uses the shape tensor:

$$\mathbf{S} = \frac{\int_V \rho(\mathbf{r})\omega(\mathbf{r})\mathbf{r}\mathbf{r}^T dV}{\int_V \rho \mathbf{r} dV}, \quad (4.12)$$

where  $\mathbf{r}$  is position from the galactic centre,  $\rho(\mathbf{r})$  is the mass density,  $V$  is the volume of an enclosed ellipsoid with the elliptical radius  $r_{\text{ell}}$ , and where the weighting function  $\omega(\mathbf{r}) = 1$ . The eigenvalues of the shape tensor correspond to  $a^2/3$ ,  $b^2/3$  and  $c^2/3$ ; where  $a$ ,  $b$  and  $c$  are the semi-principal axes; and which can be used to calculate the ellipticity as  $\epsilon = 1 - b/a$ .

However, simply calculating the shape tensor and getting the eigenvalues isn't possible, as the elliptical radius is defined, in part, using the axis ratios  $a/b$  and  $a/c$ :

$$r_{\text{ell}} = \sqrt{x_{\text{ell}}^2 + \frac{y_{\text{ell}}^2}{(b/a)^2} + \frac{z_{\text{ell}}^2}{(c/a)^2}}. \quad (4.13)$$

This means that we have to turn the calculation into an iterative process by starting with  $b/a = c/a = 1$  for the initial value of  $r_{\text{ell}}$ , and calculating new shape tensor eigenvalues using previously gained axis ratios until the values of the ratios start to converge.

We calculate  $\lambda_{Re}$  and  $\epsilon_e$ , i.e. the ellipticity at the effective radius (the ellipticity is calculated using  $r_{\text{ell}} = R_e$ , and a convergence criterion of a difference smaller  $10^{-3}$  between consequent axis ratios), for every merger simulation snapshot and plot them against each other, alongside the previously mentioned slow rotator thresholds, and observations from the ATLAS<sup>3D</sup>-survey (Cappellari et al., 2011). The resulting plot can be seen in figure 4.9.

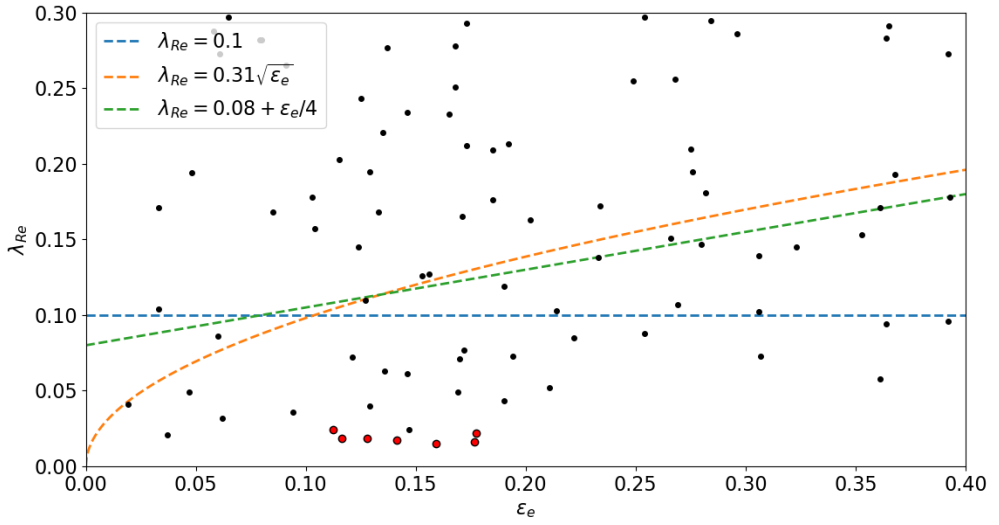


**Figure 4.9:** The values of the  $\lambda_{Re}$ -parameter of galaxies, plotted against their ellipticity at the effective radius. The red dots correspond to the simulated merger remnants, whereas the black dots correspond to galaxies observed in the ATLAS<sup>3D</sup>-survey (Cappellari et al., 2011; Emsellem et al., 2011). The dashed lines display different slow rotator thresholds as a function of ellipticity (Emsellem et al., 2007, 2011; Cappellari, 2016).

Regardless of the threshold used for differentiating between slow and fast rotators, figure 4.9 shows us that all of the simulated merger remnants are clearly classified as slow rotators. This agrees well with the kinematic anisotropies seen in the IFU maps, which also implied a slow rotator classification for the remnants.



## 4.6 Comparison to NGC 1600

As the physical properties of the merger progenitors are modelled after NGC 1600, it is interesting to see how the results from the simulations compare to actual observations. We are mainly comparing the observations to the simulated merger remnant from "Snapshot-6", as the mass of the SMBH binary in the simulation is equivalent to the assumed mass of the central SMBH in NGC 1600 ( $M_{\bullet} = 1.7 \times 10^{10} M_{\odot}$ ) (Thomas et al., 2016).

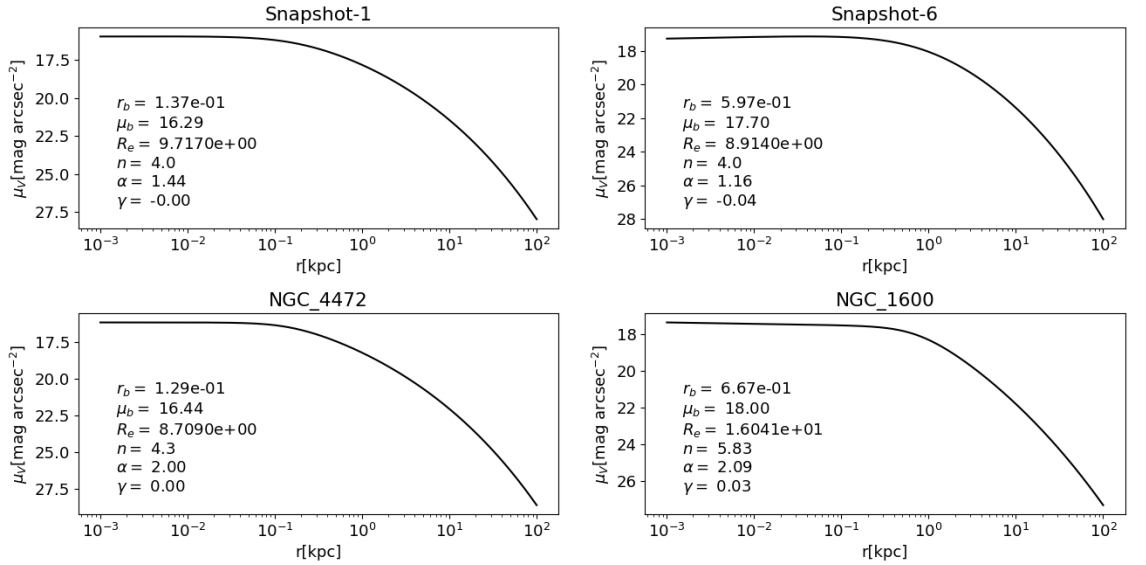


**Figure 4.10:** Core-Sérsic profile fits of surface brightness profiles, calculated from either simulated merger remnant snapshots (top figures) or observed galaxies (bottom figures). The respective fit parameters are written on the figures in units that correspond to the axes. The progenitors of the top-left simulation contained  $M_{\bullet} = 8.5 \times 10^8 M_{\odot}$  central SMBHs, where as the ones from the top-right simulation contained  $M_{\bullet} = 8.5 \times 10^9 M_{\odot}$  central SMBHs. The parameters for NGC 1600's profile (bottom right), are changed from the units used by Thomas et al. (2016) to the above, by assuming  $V - R = 0.5$  (the same assumption being done in Lauer et al. (2007b)), and by using the distance  $D = 64 \text{ Mpc}$  (Thomas et al., 2016) in order to define the relation between arc seconds and parsecs. As one can see, the profiles gained from simulations and observations are quite similar to each other.

Figure 4.10 shows the core-Sérsic profile fits of the surface brightness profiles

alongside the best-fit parameters from Snapshot-6 and NGC 1600 as well as from Snapshot-1 and NGC 4472. Comparing the profiles of Snapshot-6 and NGC 1600, one can see unmistakeable similarities. Not only are the shapes of the profiles extremely similar, apart from the larger core and effective radii the best-fit parameters are also quite closely related.

A further comparison between some of the properties of the two galaxies can be seen in table 4.4. Most importantly the table shows that even their kinematic properties are alike, or in the very least, of the same order of magnitude. Furthermore, much like the merger remnants seen in the snapshots, by looking at its  $\lambda_e$  parameter and ellipticity at the effective radius, NGC 1600 can easily be identified as a slow rotator.

Of course due to the nature in which the merger progenitors were modelled, the physical parameters being similar between the simulated merger remnant and NGC 1600 isn't unexpected. This result does however further imply that the light deficiency observed in the cores of galaxies such as NGC 1600 is formed similarly to the simulations, i.e. through a scouring process caused by a binary SMBH during a galaxy merger.

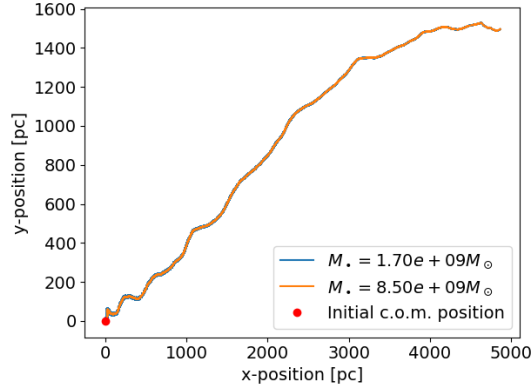
Galaxy	$M_\star$ [ $\times 10^{11} M_\odot$ ]	$M_\bullet$ [ $\times 10^{10} M_\odot$ ]	$R_e$ [kpc]	$\mu_e$ [mag/arcsec <sup>2</sup> ]	$n$	$V_{\text{LOS}}$ [km/s]	$\sigma_e$ [km/s]	$\lambda_e$	$\epsilon_e$
(1)	(2)	(3)	(4)	(5)	(6)	(7)	(8)	(9)	(10)
Snapshot-6	8.3	$2 \times 0.85$	5.507	20.26	4	6.9	311	0.024	0.11
NGC 1600	8.3	1.7	$\sim 16$	$\sim 22.8$	5.83	3.4	293	0.026	0.32

**Table 4.4:** Comparison between the physical properties of the simulated merger remnant "Snapshot-6" and the galaxy NGC 1600. The properties described in the columns are explained below, with the sources for the properties of NGC 1600 being written inside the brackets.

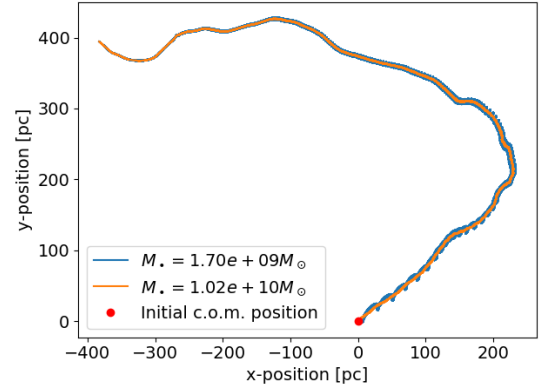
- (1) Name of the galaxy.
- (2) Total stellar mass (Thomas et al., 2016).
- (3) Central black hole mass (Thomas et al., 2016).
- (4) Effective radius (Thomas et al., 2016). For NGC 1600, the effective radius is changed from arc seconds to kpc by assuming that it is located at the distance of  $D = 64$  Mpc (Thomas et al., 2016).
- (5) Surface brightness at the effective radius. Calculated from the best fit core-Sérsic profile parameters given in Thomas et al. (2016).
- (6) Sérsic index from the best fitting core-Sérsic profile fit (Thomas et al., 2016).
- (7) Mean line-of-sight velocity inside the effective radius (Bender et al., 1994).
- (8) Velocity dispersion inside the effective radius (Veale et al., 2017). For "Snapshot-6", the given velocity dispersion is calculated from a Voronoi binned image as the mean of the velocity dispersion values of the bins located inside the effective radius.
- (9) Spin parameter at the effective radius (Veale et al., 2018).
- (10) For "Snapshot-6": ellipticity of the galaxy at the effective radius; and for NGC 1600: luminosity weighted ellipticity (Goullaud et al., 2018).

## 5. Conclusions

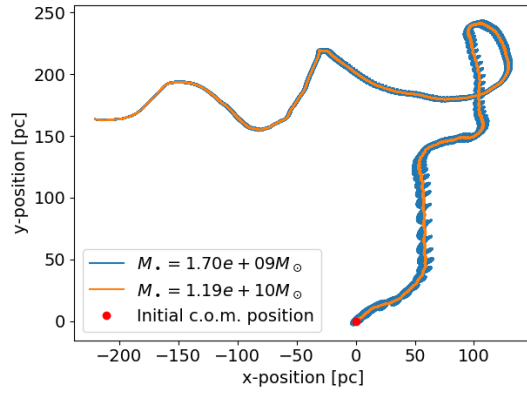
## A. Figures



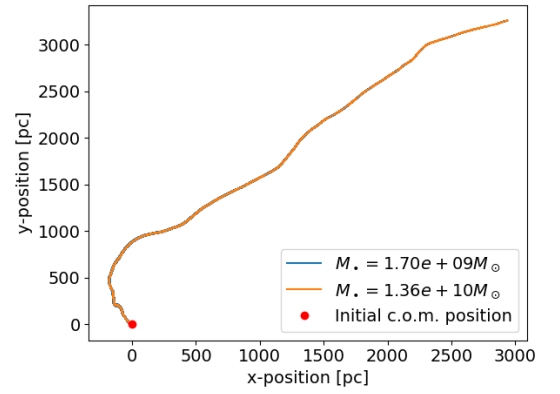
(a) Run 1



(b) Run 2



(c) Run 3



(d) Run 4

**Figure A.1:** The trajectories of the black holes from simulation runs by Mannerkoski et al. (2019). The coordinates are centred on the initial location of the centre-of-mass of the black hole system. The orange and blue lines show the paths taken by the smaller and larger black holes respectively during the simulation.

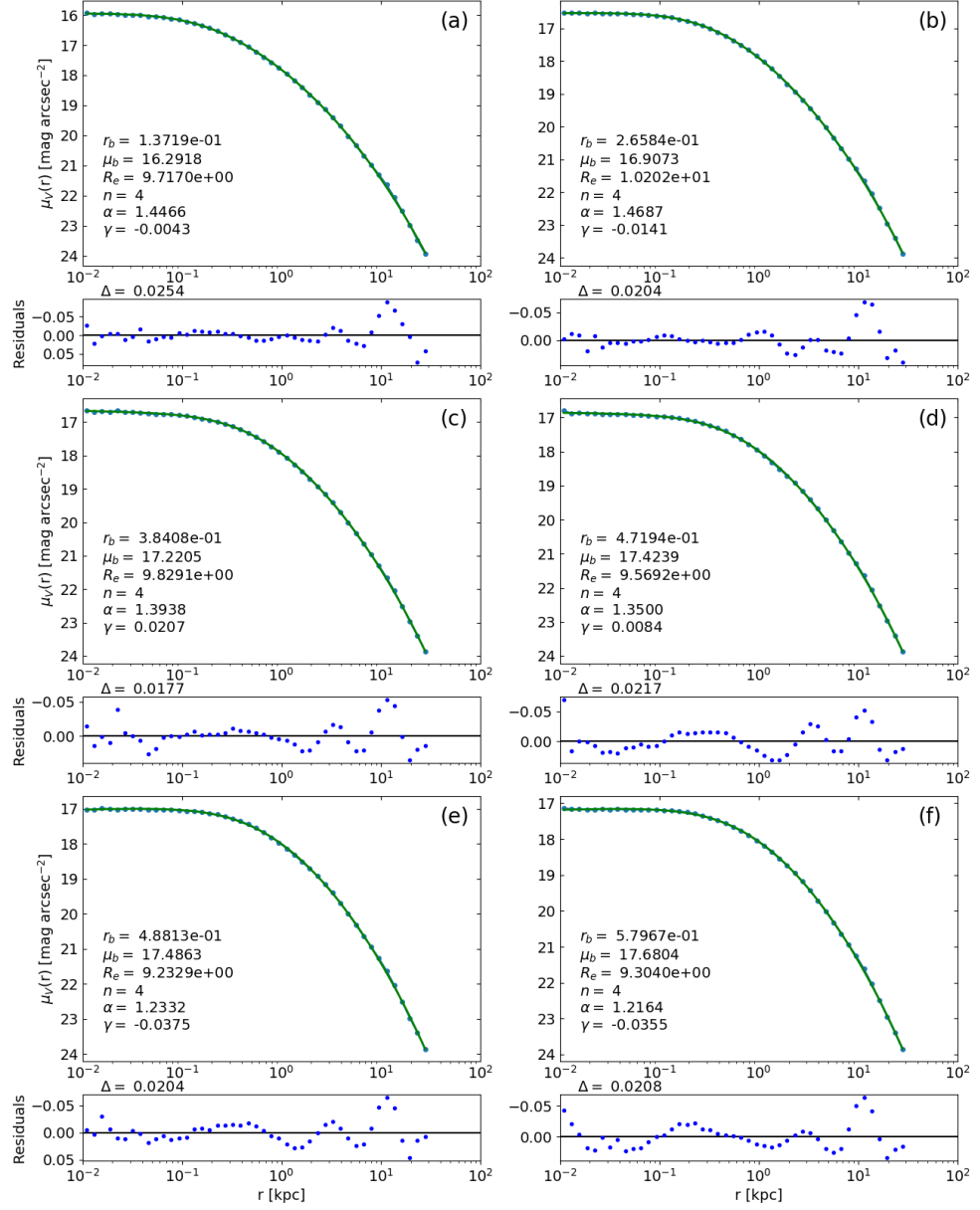


**Figure A.2:** Core-Sérsic profile fits of the surface brightness data calculated from all of the individual simulated merger remnants with progenitors containing central supermassive black holes. The letters (a)-(f) denote the different snapshots ((a): Snapshot-1, (b): Snapshot-2, (c): Snapshot-3, (d): Snapshot-4, (e): Snapshot-5, (f): Snapshot-6).

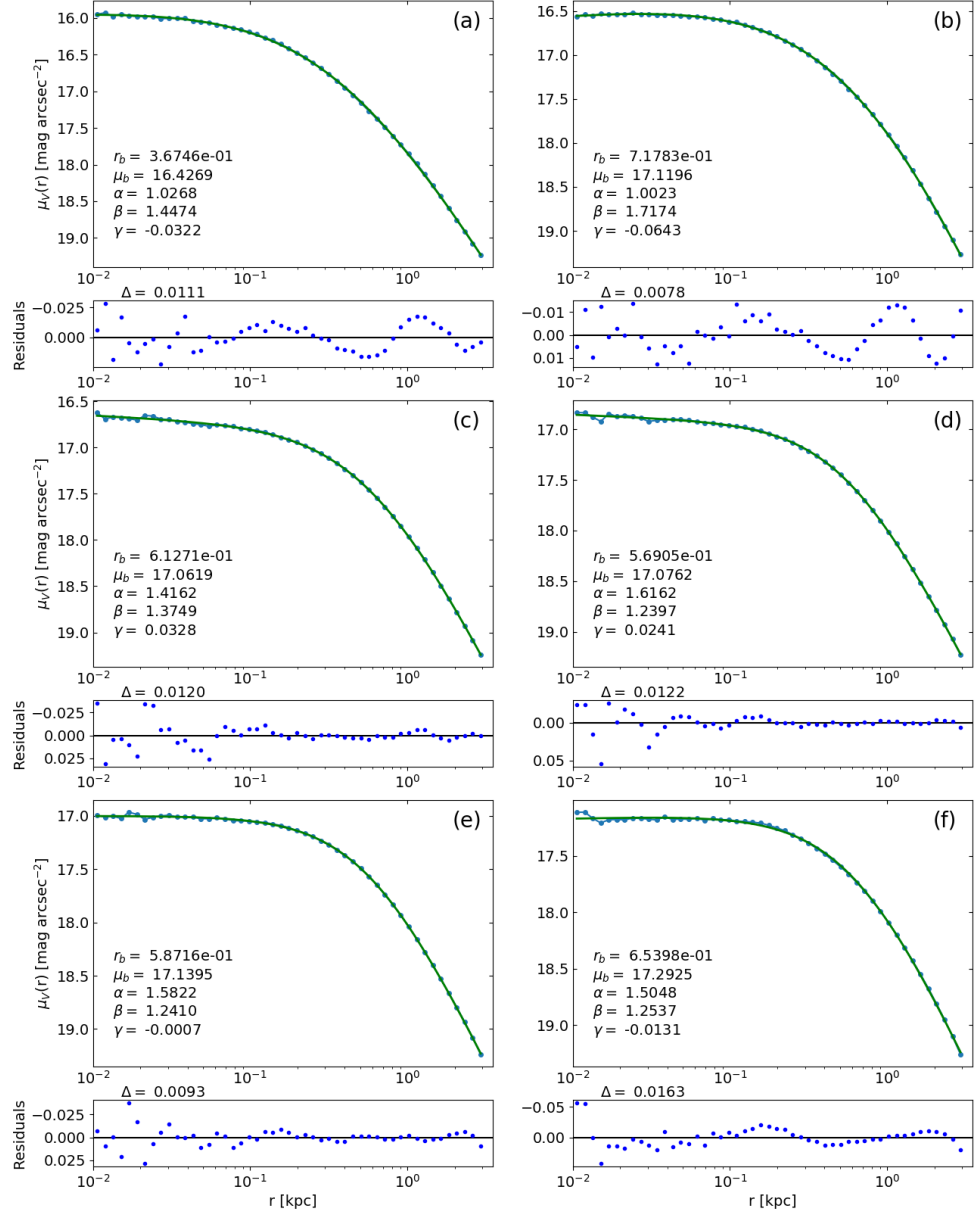


**Figure A.3:** Nuker profile fits of the surface brightness data calculated from all of the individual simulated merger remnants with progenitors containing central supermassive black holes. The letters (a)-(f) denote the different merger remnants ((a): Snapshot-1, (b): Snapshot-2, (c): Snapshot-3, (d): Snapshot-4, (e): Snapshot-5, (f): Snapshot-6).



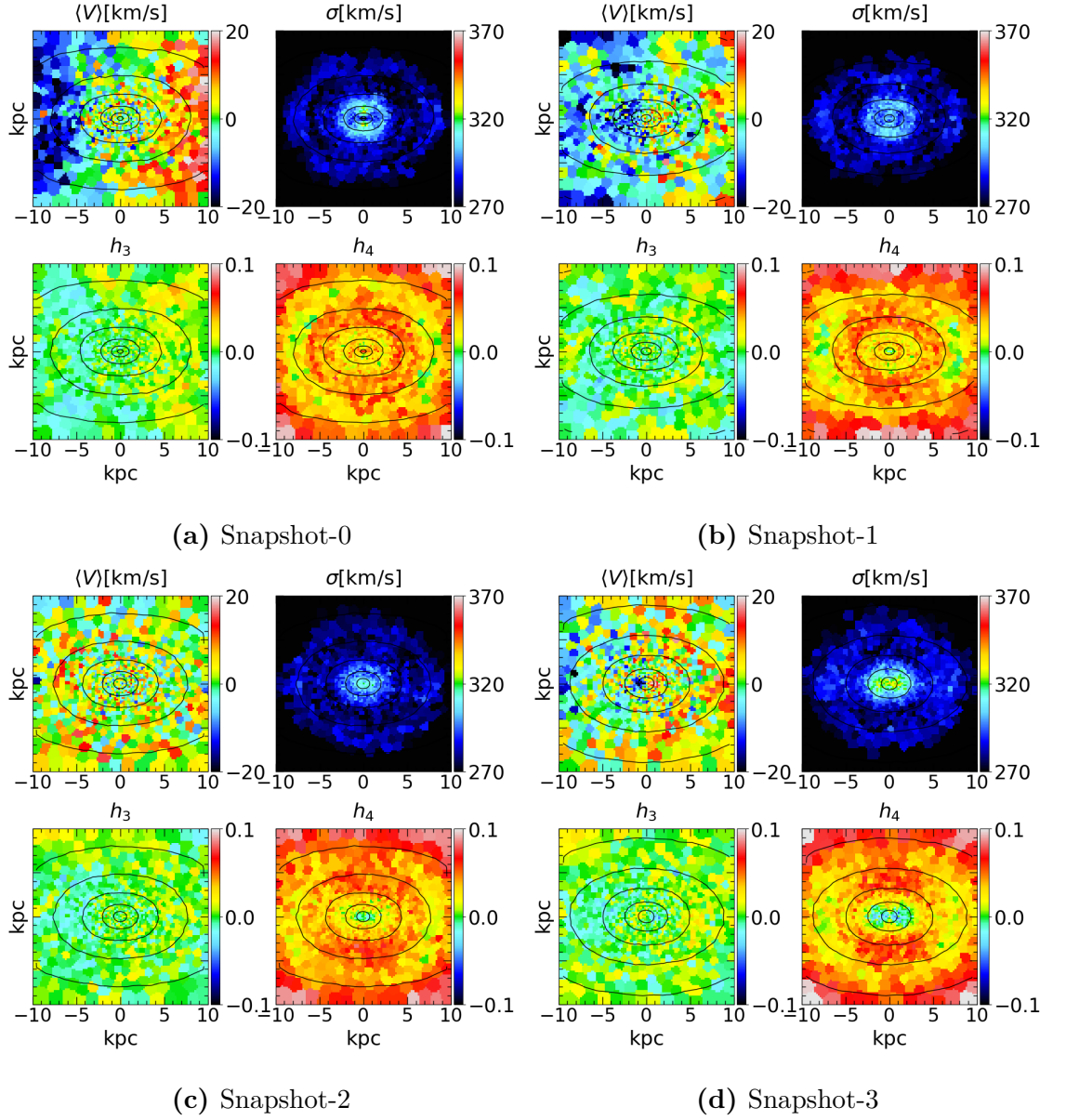
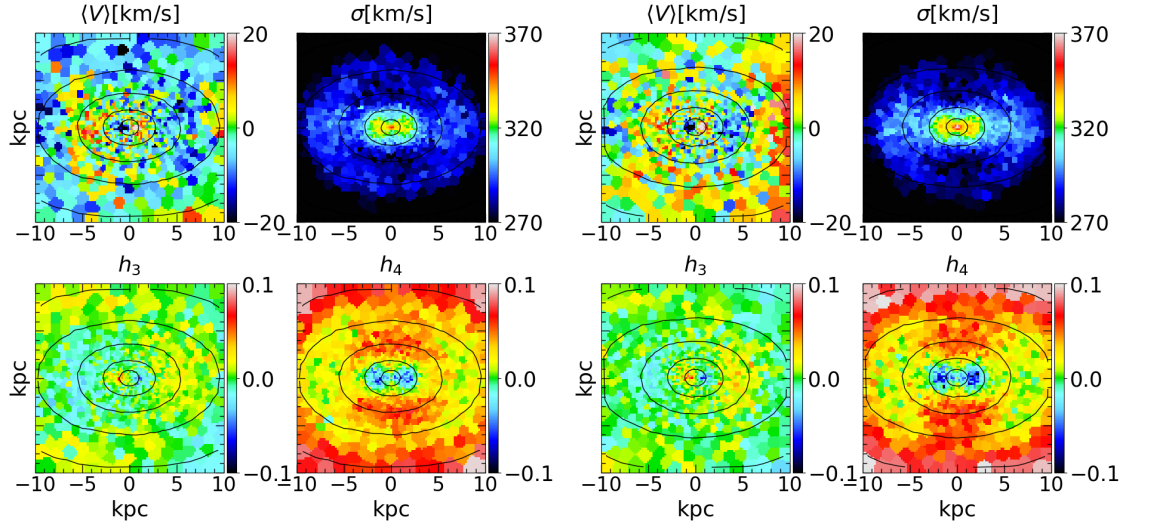
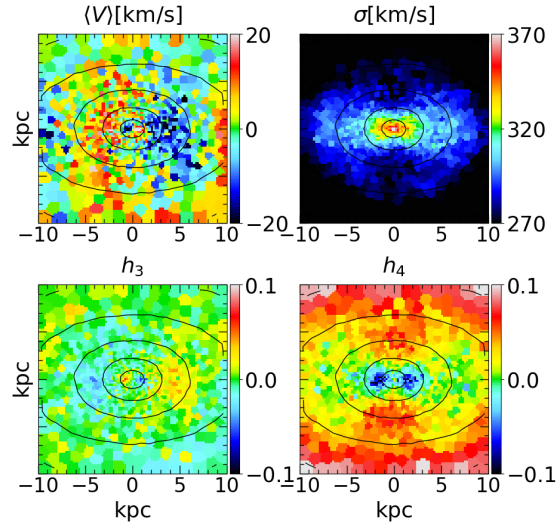


**Figure A.4:** IFU-maps of average LOS-velocities, velocity dispersion,  $h_3$  parameters and  $h_4$  parameters from four simulated merger remnants: Snapshot-0, Snapshot-1, Snapshot-2 and Snapshot-3.



(a) Snapshot-4

(b) Snapshot-5



(c) Snapshot-6

**Figure A.5:** IFU-maps of average LOS-velocities, velocity dispersion,  $h_3$  parameters and  $h_4$  parameters from three simulated merger remnants: Snapshot-4, Snapshot-5 and Snapshot-6.

# Bibliography

R. Bender, R. P. Saglia, and O. E. Gerhard. Line-of-sight velocity distributions of elliptical galaxies. *Monthly Notices of the Royal Astronomical Society*, 269: 785–813, Aug 1994. doi: 10.1093/mnras/269.3.785.

James Binney and Scott Tremaine. *Galactic Dynamics: Second Edition*. 2008.

M. Cappellari, E. Emsellem, D. Krajnović, R. M. McDermid, N. Scott, G. A. Verdoes Kleijn, L. M. Young, K. Alatalo, R. Bacon, L. Blitz, M. Bois, F. Bournaud, M. Bureau, R. L. Davies, T. A. Davis, P. T. de Zeeuw, P.-A. Duc, S. Khochfar, H. Kuntschner, P.-Y. Lablanche, R. Morganti, T. Naab, T. Oosterloo, M. Sarzi, P. Serra, and A.-M. Weijmans. The ATLAS<sup>3D</sup> project - I. A volume-limited sample of 260 nearby early-type galaxies: science goals and selection criteria. *Monthly Notices of the Royal Astronomical Society*, 413:813–836, May 2011. doi: 10.1111/j.1365-2966.2010.18174.x.

Michele Cappellari. Structure and Kinematics of Early-Type Galaxies from Integral Field Spectroscopy. *Annual Review of Astronomy and Astrophysics*, 54:597–665, Sep 2016. doi: 10.1146/annurev-astro-082214-122432.

Michele Cappellari and Yannick Copin. Adaptive spatial binning of integral-field spectroscopic data using Voronoi tessellations. *Monthly Notices of the Royal Astronomical Society*, 342(2):345–354, Jun 2003. doi: 10.1046/j.1365-8711.2003.06541.x.

- Michele Cappellari, Eric Emsellem, R. Bacon, M. Bureau, Roger L. Davies, P. T. de Zeeuw, Jesús Falcón-Barroso, Davor Krajnović, Harald Kuntschner, Richard M. McDermid, Reynier F. Peletier, Marc Sarzi, Remco C. E. van den Bosch, and Glenn van de Ven. The SAURON project - X. The orbital anisotropy of elliptical and lenticular galaxies: revisiting the  $(V/\sigma, \epsilon)$  diagram with integral-field stellar kinematics. *Monthly Notices of the Royal Astronomical Society*, 379(2):418–444, Aug 2007. doi: 10.1111/j.1365-2966.2007.11963.x.
- C. Marcella Carollo, Marijn Franx, Garth D. Illingworth, and Duncan A. Forbes. Ellipticals with Kinematically Distinct Cores: V - I Color Images with WFC2. *The Astrophysical Journal*, 481(2):710–734, May 1997. doi: 10.1086/304060.
- W. Dehnen. A Family of Potential-Density Pairs for Spherical Galaxies and Bulges. *Monthly Notices of the Royal Astronomical Society*, 265:250, Nov 1993. doi: 10.1093/mnras/265.1.250.
- Bililign T. Dullo and Alister W. Graham. Sizing up Partially Depleted Galaxy Cores. *The Astrophysical Journal*, 755(2):163, August 2012. doi: 10.1088/0004-637X/755/2/163.
- E. Emsellem, M. Cappellari, R. F. Peletier, R. M. McDermid, R. Bacon, M. Bureau, Y. Copin, R. L. Davies, D. Krajnović, H. Kuntschner, B. W. Miller, and P. T. de Zeeuw. The SAURON project - III. Integral-field absorption-line kinematics of 48 elliptical and lenticular galaxies. *Monthly Notices of the Royal Astronomical Society*, 352:721–743, August 2004. doi: 10.1111/j.1365-2966.2004.07948.x.
- E. Emsellem, M. Cappellari, D. Krajnović, K. Alatalo, L. Blitz, M. Bois, F. Bournaud, M. Bureau, R. L. Davies, T. A. Davis, P. T. de Zeeuw, S. Khochfar, H. Kuntschner, P.-Y. Lablanche, R. M. McDermid, R. Morganti, T. Naab, T. Oosterloo, M. Sarzi, N. Scott, P. Serra, G. van de Ven, A.-M. Weijmans,

- and L. M. Young. The ATLAS<sup>3D</sup> project - III. A census of the stellar angular momentum within the effective radius of early-type galaxies: unveiling the distribution of fast and slow rotators. *Monthly Notices of the Royal Astronomical Society*, 414:888–912, June 2011. doi: 10.1111/j.1365-2966.2011.18496.x.
- Eric Emsellem, Michele Cappellari, Davor Krajnović, Glenn van de Ven, R. Bacon, M. Bureau, Roger L. Davies, P. T. de Zeeuw, Jesús Falcón-Barroso, Harald Kuntschner, Richard McDermid, Reynier F. Peletier, and Marc Sarzi. The SAURON project - IX. A kinematic classification for early-type galaxies. *Monthly Notices of the Royal Astronomical Society*, 379(2):401–417, Aug 2007. doi: 10.1111/j.1365-2966.2007.11752.x.
- Charles F. Goullaud, Joseph B. Jensen, John P. Blakeslee, Chung-Pei Ma, Jenny E. Greene, and Jens Thomas. The MASSIVE Survey. IX. Photometric Analysis of 35 High-mass Early-type Galaxies with HST WFC3/IR. *The Astrophysical Journal*, 856(1):11, March 2018. doi: 10.3847/1538-4357/aab1f3.
- Alister W. Graham, Peter Erwin, I. Trujillo, and A. Asensio Ramos. A New Empirical Model for the Structural Analysis of Early-Type Galaxies, and A Critical Review of the Nuker Model. *The Astronomical Journal*, 125(6):2951–2963, Jun 2003a. doi: 10.1086/375320.
- Alister W. Graham, Peter Erwin, I. Trujillo, and A. Asensio Ramos. A New Empirical Model for the Structural Analysis of Early-Type Galaxies, and A Critical Review of the Nuker Model. *The Astronomical Journal*, 125(6):2951–2963, Jun 2003b. doi: 10.1086/375320.
- T. R. Lauer, E. A. Ajhar, Y. I. Byun, A. Dressler, S. M. Faber, C. Grillmair, J. Kormendy, D. Richstone, and S. Tremaine. The Centers of Early-Type Galaxies with HST. I. An Observational Survey. *The Astronomical Journal*, 110:2622, Dec 1995. doi: 10.1086/117719.

- Tod R. Lauer, S. M. Faber, Douglas Richstone, Karl Gebhardt, Scott Tremaine, Marc Postman, Alan Dressler, M. C. Aller, Alexei V. Filippenko, and Richard Green. The Masses of Nuclear Black Holes in Luminous Elliptical Galaxies and Implications for the Space Density of the Most Massive Black Holes. *The Astrophysical Journal*, 662(2):808–834, Jun 2007a. doi: 10.1086/518223.
- Tod R. Lauer, Karl Gebhardt, S. M. Faber, Douglas Richstone, Scott Tremaine, John Kormendy, M. C. Aller, Ralf Bender, Alan Dressler, and Alexei V. Filippenko. The Centers of Early-Type Galaxies with Hubble Space Telescope. VI. Bimodal Central Surface Brightness Profiles. *The Astrophysical Journal*, 664(1):226–256, July 2007b. doi: 10.1086/519229.
- Matias Mannerkoski, Peter H. Johansson, Pauli Pihajoki, Antti Rantala, and Naab Thorsten. Inspiral of Supermassive Black Holes In Galactic Scale Simulations. *Monthly Notices of the Royal Astronomical Society*, 856(1):11, ? 2019. doi: 10.3847/1538-4357/aab1f3.
- Miloš Milosavljević and David Merritt. Formation of Galactic Nuclei. *The Astrophysical Journal*, 563(1):34–62, Dec 2001. doi: 10.1086/323830.
- Gerald D. Quinlan and Lars Hernquist. The dynamical evolution of massive black hole binaries — II. Self-consistent N-body integrations. *New Astronomy*, 2(6):533–554, Dec 1997. doi: 10.1016/S1384-1076(97)00039-0.
- Antti Rantala, Peter H. Johansson, Thorsten Naab, Jens Thomas, and Matteo Frigo. The Formation of Extremely Diffuse Galaxy Cores by Merging Supermassive Black Holes. *The Astrophysical Journal*, 864(2):113, September 2018. doi: 10.3847/1538-4357/aada47.
- J. Thomas, R. P. Saglia, R. Bender, P. Erwin, and M. Fabricius. The Dynamical

- Fingerprint of Core Scouring in Massive Elliptical Galaxies. *The Astrophysical Journal*, 782(1):39, Feb 2014. doi: 10.1088/0004-637X/782/1/39.
- Jens Thomas, Chung-Pei Ma, Nicholas J. McConnell, Jenny E. Greene, John P. Blakeslee, and Ryan Janish. A 17-billion-solar-mass black hole in a group galaxy with a diffuse core. *Nature*, 532(7599):340–342, April 2016. doi: 10.1038/nature17197.
- Melanie Veale, Chung-Pei Ma, Jens Thomas, Jenny E. Greene, Nicholas J. McConnell, Jonelle Walsh, Jennifer Ito, John P. Blakeslee, and Ryan Janish. The MASSIVE Survey - V. Spatially resolved stellar angular momentum, velocity dispersion, and higher moments of the 41 most massive local early-type galaxies. *Monthly Notices of the Royal Astronomical Society*, 464(1):356–384, January 2017. doi: 10.1093/mnras/stw2330.
- Melanie Veale, Chung-Pei Ma, Jenny E. Greene, Jens Thomas, John P. Blakeslee, Jonelle L. Walsh, and Jennifer Ito. The MASSIVE survey - VIII. Stellar velocity dispersion profiles and environmental dependence of early-type galaxies. *Monthly Notices of the Royal Astronomical Society*, 473(4):5446–5467, February 2018. doi: 10.1093/mnras/stx2717.
- Marcel Zemp, Oleg Y. Gnedin, Nickolay Y. Gnedin, and Andrey V. Kravtsov. On Determining the Shape of Matter Distributions. *The Astrophysical Journal Supplement*, 197(2):30, December 2011. doi: 10.1088/0067-0049/197/2/30.